High-Efficiency Ion-Exchange Doping of Conducting Polymers

Ian E. Jacobs, Yue Lin, Yuxuan Huang, Xinglong Ren, Dimitrios Simatos, Chen Chen, Dion Tjhe, Martin Statz, Lianglun Lai, Peter A. Finn, William G. Neal, Gabriele D'Avino, Vincent Lemaur, Simone Fratini, David Beljonne, Joseph Strzalka, Christian B. Nielsen, Stephen Barlow, Seth R. Marder, Iain McCulloch, and Henning Sirringhaus*

Dedicated to Professor Daoben Zhu on the occasion of his 80th birthday

Molecular doping—the use of redox-active small molecules as dopants for organic semiconductors—has seen a surge in research interest driven by emerging applications in sensing, bioelectronics, and thermoelectrics. However, molecular doping carries with it several intrinsic problems stemming directly from the redox-active character of these materials. A recent breakthrough was a doping technique based on ion-exchange, which separates the redox and charge compensation steps of the doping process. Here, the equilibrium and kinetics of ion exchange doping in a model system, poly(2,5-bis(3-alkylthiophen-2-yl)thieno(3,2-b)thiophene) (PBTTT) doped with $FeCl_3$ and an ionic liquid, is studied, reaching conductivities in excess of 1000 S cm^{-1} and ion exchange efficiencies above 99%. Several factors that enable such high performance, including the choice of acetonitrile as the doping solvent, which largely eliminates electrolyte association effects and dramatically increases the doping strength of $FeCl_3$, are demonstrated. In this high ion exchange efficiency regime, a simple connection between electrochemical doping and ion exchange is illustrated, and it is shown that the performance and stability of highly doped PBTTT is ultimately limited by intrinsically poor stability at high redox potential.

1. Introduction

The simplest, most common approach to doping in semiconducting polymers, molecular doping[1–4] (**Figure 1**a) has several fundamental limitations. These arise from the requirement that the dopant molecule must perform two seemingly unrelated roles. In p-type doping, initially the dopant functions as an oxidizing agent, nearly always via a reversible electron transfer reaction, the product of which is then inserted as an ionized dopant into the film to compensate the positive charge on the polymer. Requiring a single chemical species to perform both these functions leads to several difficulties:

1) p-Type dopants are by definition strong electron acceptors (oxidizing agents), and thus quite reactive.[2,5,6] Because at equilibrium a small population of neutral dopants always exists, both redox

I. E. Jacobs, Y. Lin, Y. Huang, X. Ren, D. Simatos, C. Chen, D. Tjhe,
M. Statz, L. Lai, H. Sirringhaus
Optoelectronics Group, Cavendish Laboratory
University of Cambridge
J J Thomson Avenue, Cambridge CB3 0HE, UK
E-mail: hs220@cam.ac.uk

D. Simatos
Department of Chemistry
University of Cambridge
Lensfield Road, Cambridge CB2 1EW, UK

P. A. Finn, W. G. Neal, C. B. Nielsen
School of Biological and Chemical Sciences
Queen Mary University of London
Mile End Road, London E1 4NS, UK

G. D'Avino, S. Fratini
Grenoble Alpes University, CNRS, Grenoble INP
Institut Néel
25 rue des Martyrs, Grenoble 38042, France

V. Lemaur, D. Beljonne
Laboratory for Chemistry of Novel Materials
University of Mons
Mons B-7000, Belgium

J. Strzalka
X-Ray Science Division
Argonne National Laboratory
Lemont, IL 60439, USA

S. Barlow, S. R. Marder
School of Chemistry and Biochemistry
and Center for Organic Photonics and Electronics
Georgia Institute of Technology
Atlanta, GA 30332, USA

I. McCulloch
KAUST Solar Center
King Abdullah University of Science and Technology (KAUST)
Thuwal 23955, Saudi Arabia

I. McCulloch
Department of Chemistry
University of Oxford
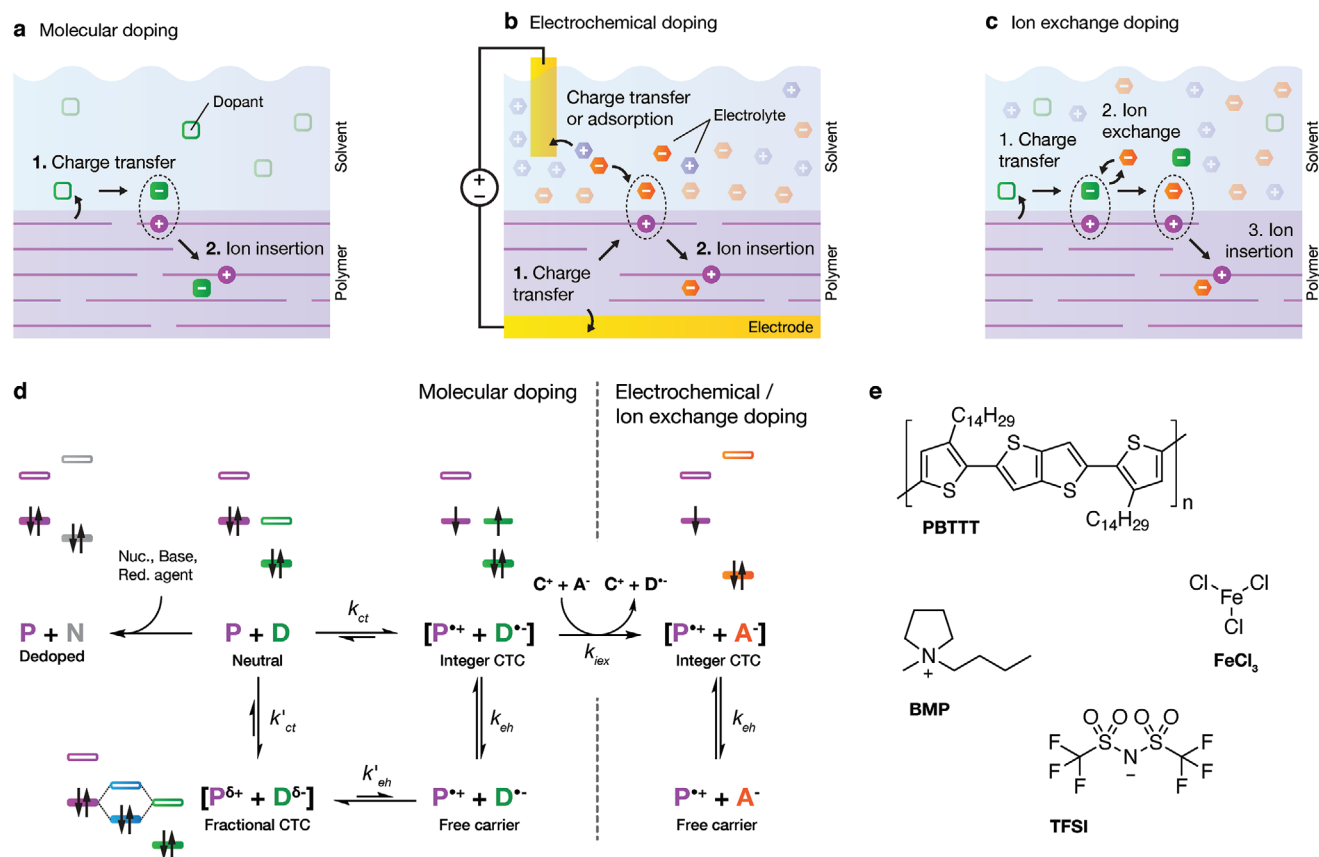12 Mansfield Road, Oxford OX1 3TA, UK

Figure 1. Doping mechanism. a) Molecular doping from an orthogonal solvent. b) Electrochemical doping. c) Ion-exchange doping. d) Reaction scheme for p-type molecular doping with ion-exchange. Representative electron configurations for each state are shown above/below; reorganization effects are neglected for clarity. e) Molecular structures of PBTTT, BMP, TFSI, and FeCl$_3$.

states of the dopant need to be chemically inert. This puts hard constraints on suitable molecular dopants.

2) The electron affinity of many dopants is significantly reduced when incorporated into an organic semiconductor[7] making it difficult to predict whether a given polymer and dopant molecule will undergo charge-transfer.

3) When the electron-transfer step is reversible, the dopant ion is inherently redox-active; p-type dopants therefore will almost always have electronic states in close vicinity to those of the polymer (Figure 1d).[1,8] In polymers there is growing evidence that integer charge-transfer is stabilized by the segregation of dopant ions to the side chain region, where π-orbital overlap with the polymer is minimized.[9–11] In contrast, when the dopant does π-stack with the polymer, fractional charge transfer complex (CTC) formation is observed.[12] Therefore, fractional CTCs are likely to form unless forbidden by symmetry or spatial separation. The bond-like character of fractional CTCs should generally make them energetically favored over ion pairs. The latter may therefore often be metastable, and fractional CTC formation likely forms a universal degradation mechanism.[13]

4) Typically most doping-induced charge carriers are strongly bound in integer CTCs, with only a small portion of charge carriers contributing to transport.[14–17] The binding energy of these states in principle can be controlled by ionic size,[2,14,18]

packing,[17] or disorder;[16,19] however the small library of dopant molecules available limits optimization.

Other classes of dopants that dope by an irreversible reaction, such as nitroso salts, can circumvent some of these problems. However, these dopants have other issues. For instance, doping the polymer poly(3- hexylthiophene-2,5-diyl) (P3HT) with NOPF$_6$ leads to much lower conductivity[20] than electrochemically doped P3HT:PF$_6$,[21] presumably due to undesirable oxidation reactions.[22] In short, we require a molecule that is a strong enough to oxidize a significant portion of the polymer sites yet gentle enough to preclude any off-target reactivity, and which leaves behind a stable counter-ion that does not disrupt the polymer microstructure but is large enough to limit trapping by integer CTCs. This is asking quite a lot from a single chemical species—the complexity of this problem has left many polymers difficult or impossible to dope to useful carrier densities and/or conductivities, while material stability remains generally poor.

There is no a priori reason why the two steps in Figure 1a—charge-transfer and charge compensation—must be performed by the same chemical species. To illustrate this point, consider the other common doping method, electrochemical doping (Figure 1b). Here, an electrode performs the charge-transfer step, while the compensating ion originates from an electrolyte

**ADVANCED
SCIENCE NEWS**

www.advancedsciencenews.com

**ADVANCED
MATERIALS**

www.advmat.de

solution and is drawn into the film to maintain charge neutrality. Although the necessity of coating the film on a working electrode limits its applicability, electrochemical doping has one major advantage over molecular doping: the ion inserted into the film can be chosen from a huge library of commercially available salts. These ions are typically closed-shell species with wide electrochemical windows,[23] that is, the ion reduction and oxidation potentials are typically separated from the redox potentials of the polymer (i.e., the onset of oxidation for p-type polymers) by several volts. This property implies that charge-transfer from the ion back to the polymer is extremely unfavorable, and that ionization efficiency in electrochemically doped films is effectively 100%. For the same reason, significant hybridization cannot occur, thus fractional CTC formation is inhibited. These two factors suggest that using closed-shell electrochemically inert counter-ions should improve the stability of highly doped films. Just as critically, the wide range of ion sizes and shapes available also potentially allow for direct tuning of Coulombic trapping[14] and structural disorder effects when the ions are incorporated into the polymer.

Yamashita et al., recently proposed a hybrid ion-exchange doping method (Figure 1c)[24] that involves adding a concentrated electrolyte to a molecular doping solution. After the initial charge-transfer step, the dopant ion exchanges with an electrolyte anion. If the exchange process is efficient, only the electrolyte counter-ion remains in the film, effectively giving a composition identical to that obtained by electrochemical doping. Thus, ion exchange forms a bridge between molecular and electrochemical doping, (k_{ex} equilibrium in Figure 1d) and combines the benefits of both techniques. Although ion-exchange has previously been applied to doped organic semiconductors,[25–28] the power of the technique was not demonstrated prior to the breakthrough by Yamashita et al. Their work convincingly demonstrated that ion-exchange can dramatically improve device stability and reach higher charge densities than typically achieved by molecular dopants.

The work of Yamashita in ref. [24] provides a clear demonstration of the potential of ion exchange doping, but it also leaves open some key questions that need to be better understood to allow a full optimization of the process and achieve higher electrical conductivities than what has been demonstrated with conventional charge transfer doping processes. One such question is the choice of the electrolyte solvent and the ionic liquid cation. Yamashita observed a strong dependence of the achievable conductivity on the ionic liquid cation. This is puzzling as the cation should in principle not be involved in the process (Figure 1c). This limited understanding has so far prevented an optimization of the process, and the highest conductivities reported in ref. [20] for the poly(2,5-bis(3-alkylthiophen-2-yl)thieno(3,2-b)thiophene) (PBTTT) model system were only 600 S cm⁻¹, which are significantly below the highest conductivities reported in molecularly doped PBTTT[29,30] or in oxidatively polymerized systems.[31] In the present work we aim to understand in more detail the key processes that govern ion exchange doping. In particular, we propose a framework that allows relating ion exchange doping to electrochemical doping, for which a large body of literature exists already. The insight gained has allowed us to optimize the process and we report here for the first time high electrical

conductivities in excess of 1000 S cm⁻¹ in ion-exchanged samples of PBTTT.

2. Results

2.1. Theory of Ion-Exchange

Ion-exchange processes have been studied for well over a century, and the theoretical basis for ion-exchange is well understood.[32] Assuming both ions are monovalent, the exchange equilibrium can be described by the molar selectivity coefficient,

$$k_{ex} = \frac{C^-_{A,f} C^-_{D,s}}{C^-_{A,s} C^-_{D,f}} \tag{1}$$

where $C^z_{i,\gamma}$ is the molar concentration of species i (dopant, D; electrolyte anion, A), in phase γ (solvent, s; film, f), with charge indicated by superscript. We define the ion-exchange efficiency as the mole fraction of exchanged counter-ions divided by the total dopant density: $x_A = C^-_{A,f}/N^+$. Substituting this into Equation (1) and rearranging gives the following expression

$$x_A = 1 - x_D = \frac{k_{ex} C^-_{A,s}}{C^-_{D,s} + k_{ex} C^-_{A,s}} \tag{2}$$

This is the ion-exchange isotherm. It describes the efficiency of the ion-exchange process at equilibrium in terms of the concentration of each ion in solution and the selectivity coefficient. Interestingly, when $C^-_{D,s} = 1$, Equation (2) is equivalent to the Langmuir isotherm, which was previously found to describe the charge-transfer equilibrium, k_{ct}, in P3HT:F4TCNQ films[2,33–35] (Section S1, Supporting Information).

We can see the impact of changing the electrolyte concentration more clearly using the identity $\Delta G^0_{ex} = -kT \log(k_{ex})$ and separating the selectivity coefficient into two terms grouped by phase,

$$\ln\left(\frac{C^-_{A,f}}{C^-_{D,f}}\right) = \ln\left(\frac{C^-_{A,s}}{C^-_{D,s}}\right) - \frac{\Delta G^0_{ex}}{kT} \tag{3}$$

The first term in the right hand side of Equation (3) describes the concentration-dependent entropy contribution resulting from ion-exchange, while the second term describes the ionic selectivity of the polymer. When $|\Delta G^0_{ex}| \le kT$, corresponding to $k_{ex} \approx 1$, the film does not show a strong preference for one ion versus the other. In this situation, the concentration of each ion can be controlled by varying the concentration ratio of electrolyte to dopant ions in solution. To achieve efficient ion-exchange, ΔG^0_{ex} must be either negative, indicating the polymer prefers the electrolyte ion, or weakly positive such that the selectivity can be overcome via the entropic term.

2.2. Exchange Efficiency in PBTTT / FeCl₃/BMP-TFSI

Our improved ion-exchange process follows a standard sequential solution doping process[33] using acetonitrile (AN) as the doping solvent, with the addition of a large excess of electrolyte.

**ADVANCED
SCIENCE NEWS**

www.advancedsciencenews.com

**ADVANCED
MATERIALS**

www.advmat.de

AN is an ideal solvent for ion-exchange doping for the same reasons as it is an ideal solvent for electrochemistry: it is extremely redox stable (electrochemical window > 6 V under anhydrous conditions), allowing us to use strong oxidants, and has a high dielectric constant ($\varepsilon_r = 36.7$)[36] allowing us to use very high electrolyte concentrations.[37] As predicted by Equation (3) and shown experimentally below, high electrolyte concentrations are critical to achieving efficient ion-exchange. We use 1-butyl-1-methylpyrrolidinium bis(trifluoromethylsulfonyl)imide (BMP TFSI) as a model ion-exchange electrolyte because it is commercially available with low water content and very high purity. The TFSI ion itself also has several properties that make it well suited as a dopant ion—it is hydrophobic, is stable under strongly oxidizing conditions, and is weakly interacting with most cations.[38]

Figure 2a shows UV–vis–NIR spectra of our model ion-exchange doping system, consisting of PBTTT thin films sequentially doped with a $FeCl_3$/acetonitrile solution (1×10^{-3} M) containing varying BMP TFSI electrolyte concentrations (1×10^{-6} M to 1 M). Molecular structures are given in Figure 2c. In all spectra, we observe complete bleaching of the polymer π–π absorbance between 2 and 3 eV and the appearance of strong P1 and P2 polaron bands in the IR (<1 and 1.5 eV,

respectively), consistent with a very high doping level. The two peaks visible in the UV at 3.2 and 3.9 eV are due to the presence of $FeCl_4^-$ anions. A spectrum of $FeCl_4^-$ in AN (dotted line, see Section S2, Supporting Information for details) is shown for comparison; the peaks are shifted slightly due to solvatochromism.

As the BMP TFSI electrolyte concentration is increased, we see a reduction in the $FeCl_4^-$ absorption due to ion-exchange along with a conductivity increase of 20% (Figure 2b, blue squares), eventually reaching values in excess of 1000 S cm^{-1}. We can extract the residual $FeCl_4^-$ concentration by fitting the UV portion of the absorption spectra (Section S3, Supporting Information). From these fits, we obtain a carrier density of $5.8 \pm 0.5 \times 10^{20}$ cm^{-3} for $FeCl_3$ doped films, corresponding to molar concentration of about 1 dopant per 1.5 PBTTT monomers. The increase in P1 band intensity suggests carrier densities in ion-exchange doped films are higher still, although precise quantification of carrier density in PBTTT:TFSI is nontrivial. A quantitative analysis of the doping level in these films will be the focus of a separate work.

The yellow circles in Figure 2b show the residual $FeCl_4^-$ concentration plotted versus BMP-TFSI concentration in the doping solution, with $FeCl_3$ solution concentration fixed at 1×10^{-3} M. Equation (2) allows us to fit these data (yellow line;
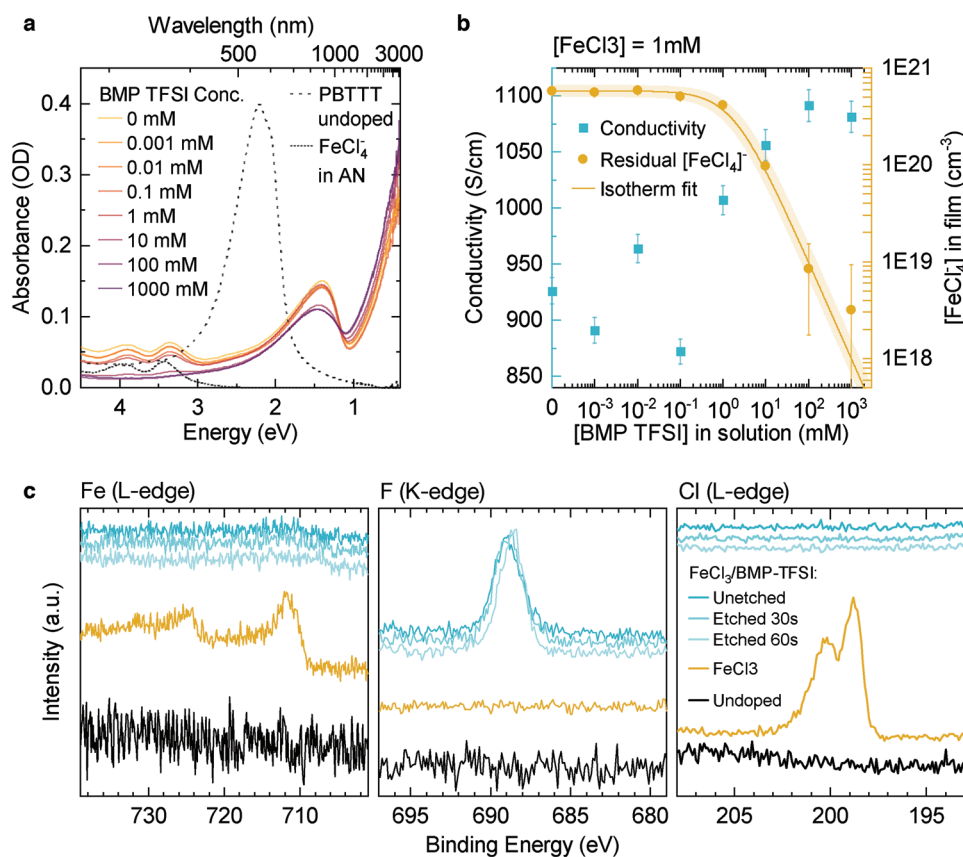

Figure 2. Ion-exchange equilibrium. a) UV–vis–NIR spectra of PBTTT films ion-exchange doped (100 s) with fixed 1×10^{-3} M $FeCl_3$ concentration and varying BMP TFSI concentration. Undoped PBTTT (dashed line) and $FeCl_4^-$ (dotted line) are shown for reference. b) Conductivity (blue squares) and residual $FeCl_4^-$ concentration (yellow circles), obtained by fitting the absorption features from the films in (a). Solid line is a fit to the ion-exchange isotherm (Equation (2)). c) XPS spectra of PBTTT thin films undoped, $FeCl_3$ (1×10^{-3} M, 100 s) doped, and ion exchange doped (BMP-TFSI/$FeCl_3$, 100/1×10^{-3} M, 100 s), showing the Fe 2p edge, F 1s edge, and Cl 2p edges. The ion exchange doped sample was remeasured after ion etching to reveal the uniformity of the film composition.

**ADVANCED
SCIENCE NEWS**
www.advancedsciencenews.com

**ADVANCED
MATERIALS**
www.advmat.de

shaded regions indicate 95% confidence interval). Using $C_{D,s}^- = 0.75 \times 10^{-3}$ M (Section S2.2, Supporting Information), we obtain $\Delta G_{ex}^0 = +29.3$ meV, indicating the polymer is weakly selective for $FeCl_4^-$. This value is roughly kT, therefore ion-exchange should be under entropic control when the electrolyte concentration is a few times higher than the $FeCl_3$ concentration.

Because the carrier density increases with increasing electrolyte concentration, using the $FeCl_4^-$ concentrations we can only calculate a lower bound on the exchange efficiency. At a 100-fold molar excess of electrolyte the exchange efficiency is at least 98%, while at a 1000-fold excess it surpasses 99%, although both of these values may be limited by our fitting routine, which is not able to accurately determine $FeCl_4^-$ concentrations below about 10^{19} cm^{-3}. To further validate our optical measurements, we used XPS to determine the elemental Fe, Cl, and F compositions of PBTTT films before doping and after $FeCl_3$ (1×10^{-3} M) or BMP-TFSI/$FeCl_3$ ($100/1 \times 10^{-3}$ M) doping (Figure 2c). These XPS data are fully consistent with our UV spectral fitting results, and confirm that $FeCl_4^-$ to $TFSI^-$ ion-exchange is highly efficient.

2.3. Importance of Doping Solvent Choice

The high carrier density and exchange efficiency achieved here derive primarily from the choice of acetonitrile (AN) as the doping solvent, as opposed to *n*-butyl acetate used in previous works.[24,39] These improvements stem from AN's high dielectric constant, which increases electrolyte dissociation, and a dramatic increase in the reduction potential of Fe^{3+} ions in AN, which enables us to reach high carrier densities.

Figure 3a (yellow line) shows a spectrum of an anhydrous 1×10^{-3} M $FeCl_3$/acetonitrile (AN) solution identical to those used in the majority of our ion exchange doping experiments. This spectrum closely matches that of the $FeCl_4^-$ anion[40,41] indicating that in solution, a considerable fraction of $FeCl_3$ exists as $FeCl_4^-$. Since AN is aprotic and has an electrochemical

window[42] extending well beyond the reduction potential of $FeCl_3$,[43] these anionic species cannot be the product of a redox reaction between $FeCl_3$ and the solvent. Instead, as described previously[44,45] $FeCl_3$ disproportionates in anhydrous AN, resulting in an equilibrium between several ligand deficient cationic species and the anionic $[FeCl_4]^-$ complex; complete disproportionation corresponds to $4FeCl_3 - >Fe^{3+} + 3[FeCl_4]^-$. Addition of excess chloride ions (Figure 3a, purple line) converts all iron in solution to to $FeCl_4^-$.[45] The magnitude of the observed increase in $FeCl_4^-$ absorption after the addition of excess chloride indicates that $FeCl_3$ almost completely dissociates to Fe^{3+} and $FeCl_4^-$ in AN (see further discussion in Section S2.2, Supporting Information).

Cyclic voltammetry measurements of $FeCl_3$ solutions in previous works have reported a rather low reduction potential, causing some confusion.[46] The observation that $FeCl_3$ dissociates to Fe^{3+} allows us to clear up these misconceptions. As a general rule, the reduction potential of iron(iii) should should tend to increase (i.e., become a stronger oxidant/p-type dopant) as more chloride ligands are removed, because the Cl^- ions donate electron density to the metal center upon complexation.[47] From the reported $Fe^{3+} \leftrightarrow Fe^{2+}$ reduction potential in aqueous solution, 0.77 V versus NHE,[48] we estimate a reduction potential of about 0.15 V versus Fc/Fc$^+$, corresponding to about -5.2 eV versus vacuum, assuming the NHE absolute electrode potential is -4.44 eV.[49,50] This would suggest that in aqueous solutions, Fe^{3+} is similar in dopant strength to F4TCNQ.

However, in anhydrous acetonitrile the $Fe^{3+} \leftrightarrow Fe^{2+}$ reduction potential was reported to be dramatically higher: a value of 1.57 V versus AgNO$_3$ for 2×10^{-3} M Fe^{3+} in anhydrous AN was reported by Kratochivil et al.[43] Assuming Fc/Fc$^+$ = 0.1 V versus Ag/Ag$^+$ in AN[51] this corresponds to a reduction potential of 1.47 V versus Fc/Fc$^+$, suggesting $FeCl_3$ in AN is a significantly stronger dopant than even CN6-CP, the strongest organic molecular dopant reported to date.[52] The reason for the strong solvent dependence of the $FeCl_3$ reduction potential
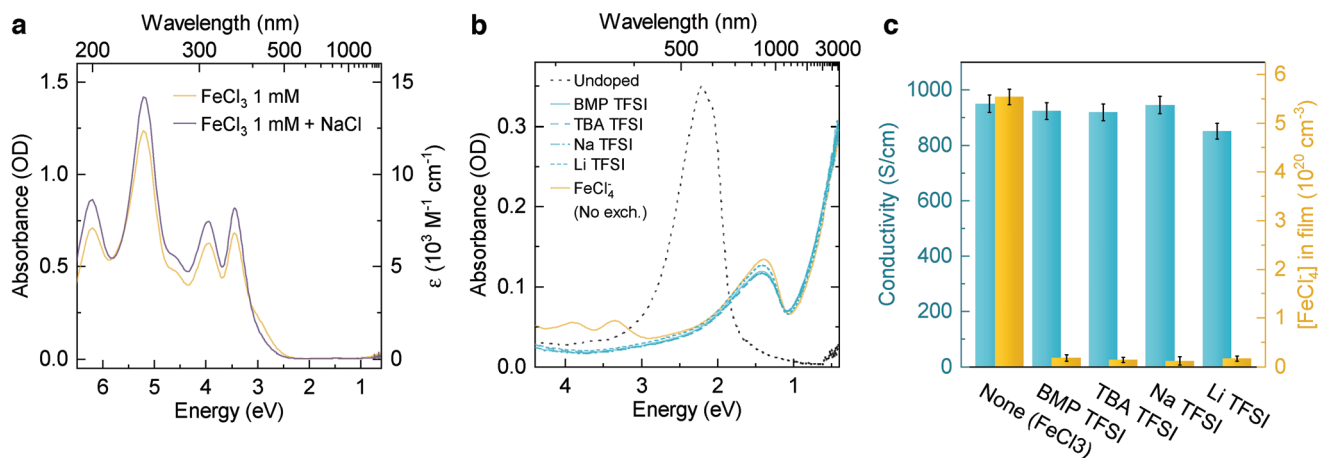

Figure 3. Details of ion exchange doping mechanism in acetonitrile a) UV–vis–NIR spectra of a $FeCl_3$ (1×10^{-3} M in AN, anhydrous), and the same solution with excess NaCl added. Spectra were taken in 1 mm path length quartz cuvettes sealed under N$_2$; AN and cuvette background have been subtracted. Right axis shows the calculated molar absorptivity (ε). b) UV–vis–NIR spectra of PBTTT films doped with varying electrolytes ($100/1 \times 10^{-3}$ M electrolyte/$FeCl_3$, AN, 300 s). Spectra of undoped PBTTT and PBTTT:$FeCl_4$ (1×10^{-3} M $FeCl_3$, AN, 300 s) shown for reference. c) Conductivity (blue, left axis) and extracted $FeCl_4^-$ concentration (yellow, right axis) for films shown in (b).

**ADVANCED
SCIENCE NEWS**

www.advancedsciencenews.com

**ADVANCED
MATERIALS**

www.advmat.de

is complex, but likely derives from a combination of factors, including a larger crystal field splitting in AN versus water that stabilizes the Fe^{2+} state, and the dielectric constant of AN, which is lower than that of water and therefore destabilizes the Fe^{3+} state relative to water, but is still high enough to permit strong dissociation of $FeCl_3$.[43] The addition of small water impurities to $FeCl_3$ in AN was reported to lower the reduction potential considerably, even in the presence of acid to prevent coordination by hydroxide ions.[43] This observation is consistent with our CV measurements of $FeCl_3$ solutions which showed a reduction potential 0.8 ± 0.08 V, slightly higher than CN6-CP (Section S2, Supporting Information). These findings indicate that water does not simply reduce the concentration of Fe^{3+}, for which the Nernst equation predicts a much weaker effect (59 mV decade^{-1}), but instead homogeneously decreases the oxidative strength of the solution without strongly affecting the concentration. To achieve high carrier densities, it is therefore critical that these solutions are prepared under dry conditions and used promptly, as AN is strongly hygroscopic.

The high dielectric constant of AN also enhances ion exchange efficiency. Previous implementations[24] of ion exchange doping used a relatively non-polar doping solvent, n-butyl acetate ($\varepsilon_r = 5$). In low dielectric solvents, Coulomb interactions between electrolyte cations and anions are $\gg kT$, resulting in an effective free anion concentration that is considerably lower than the electrolyte concentration. In Yamashita et al., this effect manifested as an exchange efficiency that depended strongly on the electrolyte cation size.[24]

In a polar solvent such as AN ($\varepsilon_r = 38$), the Coulomb interaction is dramatically weaker, and the electrolyte ions should be nearly fully dissociated at the high concentration used for ion exchange.[53] Under these conditions, the electrolyte cation is simply a spectator and plays no role in the doping process; the overall reaction is therefore equivalent to doping with Fe(III) TFSI[54] but with the flexibility to use different anions. Figure 3b shows UV–vis–NIR spectra of PBTTT films ion-exchange doped with several different cation:TFSI electrolytes ($100:1 \times 10^{-3}$ M electrolyte:$FeCl_3$, AN). We observe similarly high ion-exchange efficiency to within error with all cations (Figure 3c), in contrast with the results of Yamashita et al.[24] A very slightly lower doping level and electrical conductivity (Figure 3c) is observed in Li TFSI presumably due to its higher water content (specified as 1%) which reduces the reduction potential of Fe^{3+}, as discussed previously. However for all cations, the conductivities obtained here are significantly greater than the value of about 600 S cm^{-1} obtained in ref. [24].

2.4. Kinetics of Ion Exchange Doping

In the theory of ion exchange given in the preceding sections, we assume the system is at equilibrium. Therefore, it is critical to understand the kinetics of both the charge transfer and ion exchange processes to ensure our measurements are performed on samples which have fully equilibrated. **Figure 4** shows UV–vis–NIR and FTIR spectroscopy, along with conductivity and grazing-incidence wide-angle X-ray scattering (GIWAXS) data for PBTTT films ion exchange doped for varying times using

our standard ion exchange process ($100/1 \times 10^{-3}$ M BMP TFSI/$FeCl_3$, AN).

UV–vis–NIR spectra (Figure 4a) show a continuous bleaching of the polymer π–π^* band, with nearly complete bleaching at 10 s and further slow bleaching continuing up to 60 s. The P1 band (<1 eV) increases continuously over the entire time period, while the P2 band (1.5 eV) peaks at 6 s and then slowly decreases with extended doping times. The decrease in P2 at high doping levels is consistent with previous reports in organic electrochemical transistor (OECT) devices at high doping levels in PBTTT,[55] and electrochemically doped P3HT films[21] where this decrease was assigned to bipolaron formation. However, the bipolaron band is generally understood to appear at a wavelength intermediate between P1 and P2,[56] while no such band is observed here.

The FTIR spectra (Figure 4b) likewise show no evidence of bipolaron formation. At short doping times (≤ 3 s) the P1 band is centered at higher energy (≈ 0.3 eV) with a weak shoulder below 0.2 eV; these two features correspond to intrachain and interchain transitions, respectively.[57] At longer doping times, above 10 s, we observe a red shift in the P1 band, which is eventually dominated by the low energy, interchain feature at long doping times (i.e., high carrier densities). The continuous redshift and increase in P1 band intensity is consistent with increasing polaron delocalization at high carrier density; we observe no signatures which can be attributed to bipolarons. It is plausible that the reduction in P2 band intensity could presumably arise from a weakening of the oscillator strength of this transition due to changes in polymer structure or doping level; similar effects were recently described by Spano and co-workers for the P1 band.[57] However a more detailed theoretical interpretation of these results will be required.

We observe a plateau in conductivity (Figure 4c) above 100 s despite spectroscopic evidence for further carrier density increases above 100 s in both UV–vis and FTIR (Figure 4a,b). Neusser et al., observed similar behavior in electrochemically doped P3HT, concluding that the plateau in conductivity corresponds to region of coexisting polaron and bipolaron states,[21] However, the absence of bipolaron signatures in our data calls this picture into question. This behavior could also potentially arise from polymer degradation under strongly oxidizing potentials, as discussed in the following section, or a relatively energy-independent density of states at high doping levels. A detailed study of the conductivity of these materials will be published separately.

In both sets of spectroscopic data, there is clear change in behavior occurring at about 6 s: the P2 intensity reaches a maximum at 6 s, while the P1 intensity increases dramatically and strongly redshifts. This is correlated with transitions observed in the conductivity, $FeCl_4^-$ concentration, and GIWAXS structural data (Figure 4c). At short doping times, below 3 s, the lamellar stacking distance remains about 21 Å—nearly the same as undoped PBTTT (20.2 Å) and much smaller than observed in highly doped PBTTT:TFSI (26.5 Å) or PBTTT:$FeCl_4$ (24.1 Å). This short stacking distance, along with the sizable charge carrier density visible in the UV–vis spectrum, implies preferential doping of grain boundaries or crystalline defect sites. The $FeCl_4^-$ concentration reaches a peak at 3 s, indicating that in this regime the exchange efficiency is quite low and that
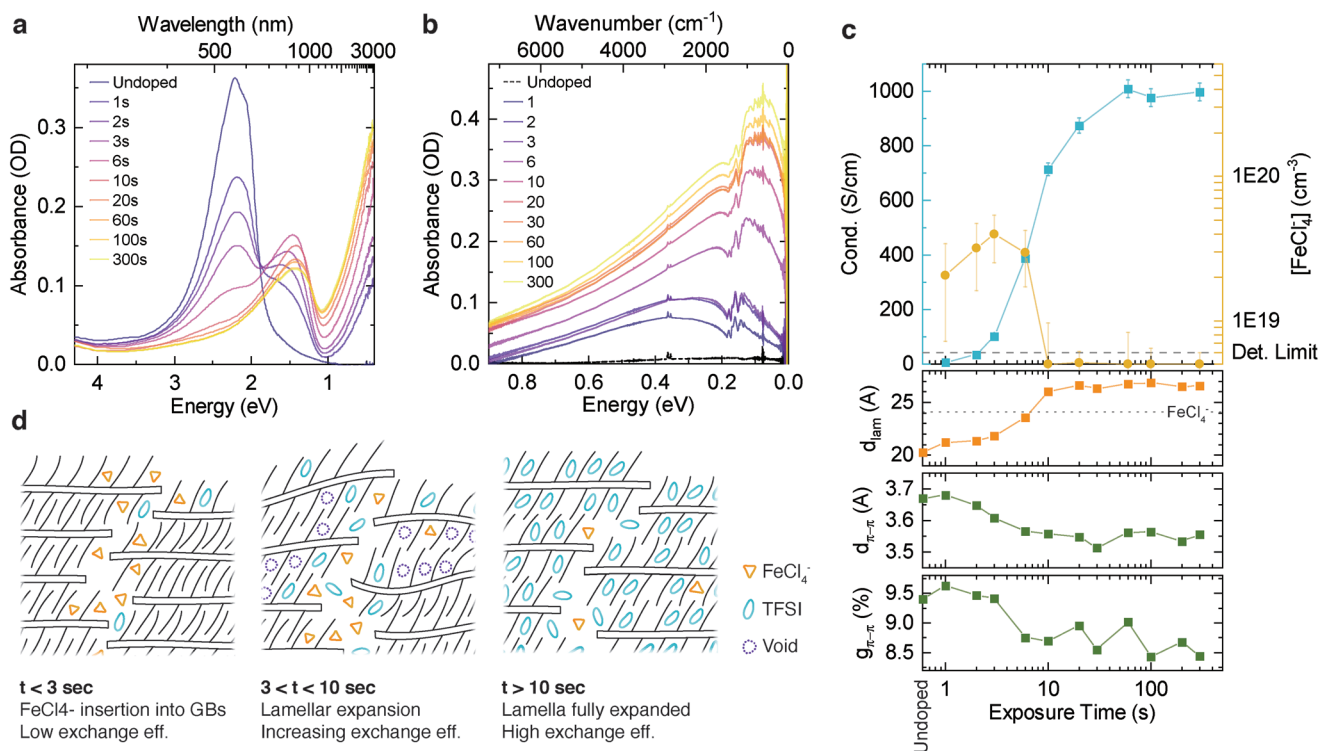
Figure 4. Kinetics of ion exchange doping. Doping solutions consisted of $100/1 \times 10^{-3}$ M BMP TFSI/FeCl$_3$ in AN. a) UV–vis–NIR spectra. b) FTIR spectra. c) Electrical conductivity, residual FeCl$_4^-$ (extracted from UV–vis spectra), unit cell parameters, and π–π paracrystallinity (extracted from GIWAXS data) as a function of doping time. d) Illustration of film microstructure at different doping times.

FeCl$_4^-$ ions penetrate the film more quickly, presumably due to their smaller size.

However, above 6 s the concentration of FeCl$_4^-$ in the film drops dramatically, indicating that the rate of TFSI ion insertion becomes much faster than FeCl$_4^-$. The persistently low FeCl$_4^-$ concentration in this regime, even as the doping level continues to increase, implies two things. First, ion exchange has clearly become much more efficient than at earlier times, and thus the equilibrium ΔG_{ex}^0 obtained previously appears to be more positive at early stages of the doping process. Second, the sharp drop in FeCl$_4^-$ concentration implies that the ion exchange equilibrium is established more quickly than the redox process, and therefore that the overall doping rate is limited by the redox step.

The observed change in behavior at 6 s appears to be driven by a sudden expansion in the lamellar stacking distance, which increases from about 21 to 26.5 Å between 3 and 10 s (Figure 4c). The rapidity of this change is suggestive of a structural phase transition in which the intercalation of ions into the lamella generates voids in neighboring sites, greatly increasing the rate of ion intercalation. An illustration of this mechanism is shown in Figure 4d. Similar behavior in an OECT device was recently observed by Bischak et al.[58] This nucleated ion-intercalation behavior can be understood as resulting from an interaction between the energetic cost of distorting the polymer crystal to incorporate an ion and the polymer oxidation potential. After an initial ion intercalates, adjacent sites become easier to oxidize because the lamella nearby are already partially "unzipped." We can see further evidence for

this phase transition in the broadening of the lamellar stacking peaks observed in the 6 s GIWAXS linecuts (Section S4, Supporting Information), consistent with heterogeneous FeCl$_4^-$ and TFSI dominated domains. The polymer π-stacking behavior also shows a sharp drop in paracrystallinity at 6 s doping time, consistent with a sudden increase in doping within crystalline domains. This effect is due to backbone planarization driven by polaron delocalization, visible as the redshift of the FTIR spectra discussed previously. Reducing the doping solution concentration while maintaining a fixed BMP TFSI/FeCl$_3$ ratio and 100 s doping time (Section S5, Supporting Information) likewise shows a drop in exchange efficiency. This further indicates that the observed low exchange efficiency prior to lamellar expansion is due to an increase in ΔG_{ex}^0, rather than slow ion exchange kinetics.

We can understand the role of crystallinity on ion exchange in a more quantitative sense by considering how our measured ΔG_{ex}^0 of +29.3 meV at high doping level compares to the reported crystallization enthalpy of PBTTT. McCulloch et al., report a cooling enthalpy of 26.5 J g^{-1}, corresponding to 192 meV per monomer, for the terrace-phase transition of PBTTT.[59] Therefore, at high doping level the energetic cost of FeCl$_4^-$ to TFSI exchange is already 10–15% of the crystallization enthalpy of PBTTT. At very low doping levels, the lattice distortion generated by an isolated TFSI ion will necessarily disrupt a number of nearby monomers due to the stiffness of the crystalline lattice; however, the energetic cost of this distortion is borne by a single ion. Therefore, we would expect ΔG_{ex}^0 to decrease as doping level increases, since the lattice distortions generated by

ADVANCED
SCIENCE NEWS
www.advancedsciencenews.com

ADVANCED
MATERIALS
www.advmat.de

the initial ions can be shared by subsequently exchanged ions (Figure 4d).

In softer or more disordered lattices these distortions become more localized, and the energetic cost of generating these distortions becomes smaller. We can see evidence for this in the ion exchange kinetics of P3HT (Section S6, Supporting Information), which is understood to have disordered side chains in contrast with the highly interdigitated side chains of PBTTT.[60] This system shows no evidence of a phase transition, reinforcing our understanding of the connection between crystalline order and ΔG^0_{ex}.
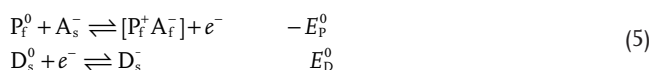
Together, these results give a clear insight into the microscopic mechanism of ion exchange doping in PBTTT revealing a clear doping level dependence of exchange efficiency. These findings suggest that in the ideal regime where electrolyte association does not limit the ion exchange efficiency, ΔG^0_{ex} is primarily controlled by the energetics of distorting the polymer crystal to incorporate the ion.

2.5. Comparison with Electrochemical Doping

When the electrolyte concentration is sufficiently high that the electrolyte ion insertion dominates (i.e., the ion-exchange efficiency is high), the overall ion-exchange reaction is simply an ion insertion reaction coupled with a redox reaction between the oxidizing agent D, (i.e., the molecular dopant and the polymer P,

$$P^0_f + A^-_s + D^0_s \overset{k_{tot}}{\rightleftharpoons} [P^+_f A^-_f] + D^-_s \tag{4}$$

For clarity, we can decompose this reaction into two half-cell reactions,

$$
\begin{aligned}
P^0_f + A^-_s &\rightleftharpoons [P^+_f A^-_f] + e^- & -E^0_P \\
D^0_s + e^- &\rightleftharpoons D^-_s & E^0_D
\end{aligned}
\tag{5}
$$

The first reaction corresponds exactly to electrochemical doping with an applied potential E^0_P, while the second reaction is the solution-state reduction potential E^0_D of the dopant molecule measured by for example, cyclic voltammetry (CV). At equilibrium, $E^0_D - E^0_P = 0$; therefore, the doping level generated by ion-exchange corresponds precisely to that prepared by electrochemical doping equilibrium with an applied voltage equal to the reduction potential of the dopant. For further discussion, see Section S1.3, Supporting Information. In this sense, we expect that any strong oxidizing agent should be capable of doping polymer films via ion exchange, and that the achievable carrier density and conductivity should depend only on the oxidizer's reduction potential, so long as the exchange efficiency remains high.

Here, we study PBTTT films ion exchange doped using 12 different dopants with reduction potentials from −0.25 to 1 V versus Fc/Fc+, shown in **Figure 5**a. All samples used the same ion exchange doping conditions: 100×10^{-3} M BMP TFSI/1×10^{-3} M dopant, 100 s exposure time. UV–vis–NIR spectra (Figure S10, Supporting Information) indicate that ion-exchange efficiency remains high across all the oxidizing

agents studied here. Figure 5c shows the electrical conductivity of each of the ion-exchange doped films in Figure 5b plotted against the reduction potential of the dopant used to prepare each film (see CV measurements in Section S2.1, Supporting Information). For comparison, we also show the conductivity of a PBTTT OECT gated using the same electrolyte (100×10^{-3} M BMP TFSI) used for ion-exchange. We observe good qualitative agreement between the electrochemical device and our ion-exchange data, consistent with our analysis above.

Electrodes typically behave as completely innocent oxidizing agents, meaning that they participate in outer-shell electron-transfer reactions only.[22] However, chemical redox agents, products of chemical redox reactions, or the electrolyte itself may participate in other types of reactions with the polymer, such as proton transfer, substitution, or elimination reactions. In general, we would expect these types of reactions to degrade the functional properties of the polymer by introducing disorder. In this sense, the quantitative mismatch between the OECT and ion-exchange data suggests that conductivity is limited by both chemical degradation by dopants and by intrinsic polymer instability.

To quantify such non-innocent behavior, we collected UV–vis spectra of each sample before doping and after dedoping with a diethylamine/acetone solution, which was previously shown to quantitatively dedope P3HT:F4TCNQ films.[5] Assuming the films are initially undoped and the oxidizing agent is completely innocent, the π–π* band intensity after dedoping should recover to the same value as measured before doping. A decrease in recovered π–π* absorbance therefore is a signature of irreversible side reactions.

Figure 5d shows the recovered π–π* absorbance for each sample. Within a given oxidizing strength range, there is a strong correlation between higher conductivity and higher π–π* recovery, for instance comparing Mo(tfd-COCF$_3$)$_3$ and Mo(tfd)$_3$, Cu(OTf)$_2$ and CAN, or CN6-CP and FeCl$_3$, indicative of varying degrees of non-innocent oxidation reactions. Furthermore, we observe a clear reduction in π–π* band recovery with increasing oxidizing agent strength, suggestive of an intrinsic polymer instability at high redox potentials.

We see direct evidence for this intrinsic polymer degradation in the OECT data (Figure 5d). During the OECT measurement, the device must be held at each gate voltage for a period before measurement to allow for formation of the electrochemical double layer and diffusion of electrolyte anions into the bulk of the polymer film. The device conductivity versus gate voltage may plateau or decrease at high gate voltages due to a decrease in mobility or density of states at the Fermi level (in degenerate systems) at high carrier density, even in the absence of any polymer degradation. However, if no degradation occurs, we should see a purely monotonic increase in conductivity with increasing gate hold time (at potentials below the maximum device conductivity), and the maximum achievable conductivity should be independent of gate hold time. Our measurements, in contrast, show that conductivity reaches a peak at 100 s hold time (Figure 5d, inset) with a strong decline in conductivity and increase in hysteresis at longer hold times–a clear signature of polymer degradation. This reactivity must originate from the polymer itself, as the electrolyte itself is stable against reduction potentials exceeding 2 volts versus Fc/Fc+. Because this

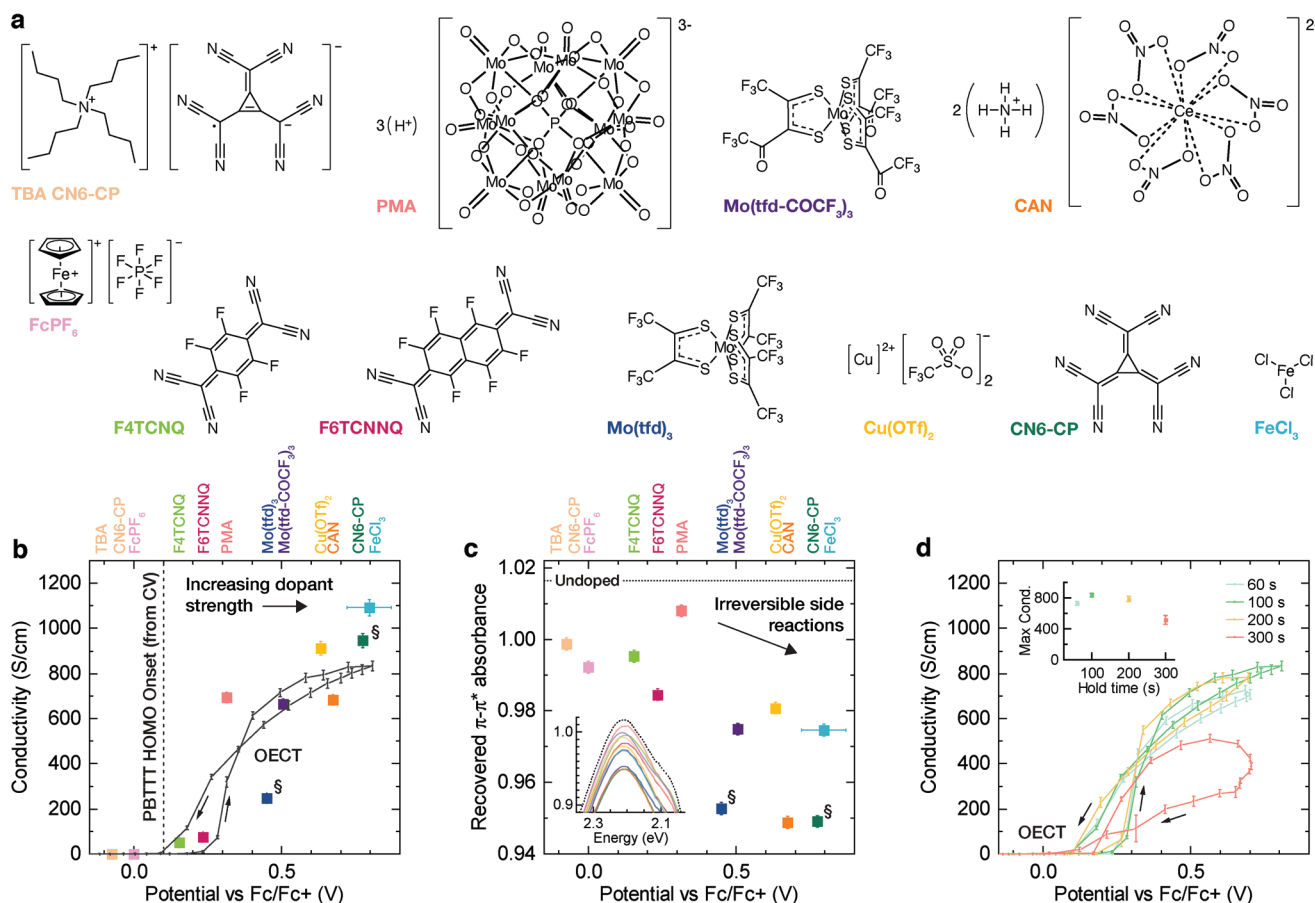**Figure 5.** Comparison with electrochemical doping. a) Chemical structures of dopants used in this study. b) Plot of conductivity versus dopant reduction potential (vs Fc/Fc+), for ion-exchange doped PBTTT films and a PBTTT OECT. Both ion-exchange and OECT devices use a 100×10^{-3} M BMP-TFSI/AN electrolyte. Dopant concentration and exposure time was 1×10^{-3} M and 100 s, respectively. Vertical dashed line shows the oxidation onset for PBTTT (corresponding to the HOMO level edge) measured by CV. c) Recovered π–$\pi*$ absorbance after chemically dedoping films in (b), normalized by each film's as cast π–$\pi*$ absorbance; inset shows the normalized dedoped spectra. The dotted line labeled "undoped" indicates the increase in π–$\pi*$ band intensity observed when an undoped film is treated with the same dedoping solution; this increase is due to removal of doping impurities.[5] § indicates the dopant displayed limited solubility in AN ($<1 \times 10^{-3}$ M). d) Conductivity versus redox potential for OECT devices gated for varying gate hold times at each data point; inset shows the maximum conductivity reached as a function of hold time.

degradation is cumulative—that is, the conductivity at high potentials is limited by the degradation built up during the scan through lower potentials—the conductivity in our OECT devices is lower than achievable via ion-exchange.

At very high doping levels there is therefore a trade-off between the time required to inject the compensating ions and the timescale of degradation reactions. In our optimized ion-exchange process using FeCl₃, device conductivity is stable for doping times from 60 to 300 s (Figure 4c). Therefore, degradation seems to be relatively slow on the timescale required to reach doping equilibrium, although the plateau in conductivity could still result from a competition between further carrier density increases and a reduction in mobility due to degradation.

Our measurements of doped film stability in nitrogen, air, and under thermal stress (Section S7, Supporting Information) echo the above findings. Although ion exchange does improve the stability of doped films, we observe significant degradation even at temperatures well below those at which TFSI-based ionic liquids typically decompose. The intrinsic instability

of highly doped PBTTT observed here is consistent with our observation of only moderate improvement in environmental stability. Our findings indicate that ion exchange provides a clear path forward in engineering highly doped and stable polymer films, but that the identification of intrinsic polymer degradation mechanisms under electrochemical stress, or in the presence of environmental impurities like water, are critical next steps in engineering highly conductive and stable polymer films.

3. Conclusions

We have demonstrated that ion-exchange doping with FeCl₃ can generate highly ordered polymer films with extremely high doping levels. We find that the process is extremely efficient in acetonitrile because its high dielectric constant allows the ionic liquid cation to behave as a mere spectator ion. In this regime, ion exchange efficiency can be controlled entropically simply by adjusting the electrolyte concentration, even in situations

where the free energy for ion exchange is weakly positive. We have also shown that the ion exchange process can essentially be understood as analogous to electrochemical doping wherein the redox potential of the dopant plays the role of the applied electrical voltage. This improved understanding reported in our work has allowed the optimization of the achievable electrical conductivity of ion-exchange doped PBTTT films, for which we have reported conductivities in excess of 1000 S cm^{-1}. It also paves the way for fundamental studies of charge transport in ion-exchange doped conjugated polymers, which make use of the broad choice of the size and shape of the ionic liquid anions that are now available to tune the electrostatic interactions between the mobile polarons on the polymer and the counterions. Ion exchange doping is an important approach that is likely to become widely used to control the electrical properties of conjugated polymers.

4. Experimental Section

Materials: PBTTT was synthesized as described previously.[59] P3HT was purchased from TCI. Ion-exchange salts Li-TFSI (>99%, <1% water), Na-TFSI (>97%), BMP-TFSI (>98.5%, <0.04% water), and TBA-TFSI (>99%) were purchased from Sigma Aldrich. Dopants PMA (hydrated, ACS reagent), Fc-PF$_6$ (>97%), Cu(OTf)$_2$ (>98%), FeCl$_3$ (anhydrous, >99.99% trace metals basis), OA, and CAN (>99.99% trace metals basis) were purchased from Sigma Aldrich. F4TCNQ (>98%) was obtained from TCI. TBA CN6-CP, F6TCNNQ, Mo(tfd)$_3$, Mo(tfd-COCF$_3$)$_3$, and CN6-CP were synthesized as described previously.[52,61–65] Anhydrous acetonitrile (Romil Hi-Dry, <20 ppm water) was used to prepare all doping solutions, while anhydrous dichlorobenzene and chlorobenzene (Romil Hi-Dry, <20 ppm water) were used for polymer solution preparation; further details are given below. Acetone and diethylamine for dedoping experiments were obtained from Romil and Sigma Aldrich, respectively. All materials were used as received.

Solution Preparation: Solutions of PBTTT were prepared in 1,2-dichlorobenzene (DCB) at a concentration of 10 mg mL^{-1} and heated at 80 °C overnight before use. Stock electrolyte solutions (1 M in AN) were prepared before use and stored in the glovebox until needed; dopant solutions (10 × 10^{-3} M) were prepared immediately before use. All polymer and doping solution preparation, including weighing reagents, was performed in an inert atmosphere (<1 ppm H$_2$O, O$_2$ during solution preparation; <10 ppm H$_2$O, O$_2$ during weighing).

Sample Preparation: Glass substrates (Corning Eagle XG) for conductivity and UV–vis measurements were cut into 1 cm squares, and 1 mm electrical contacts (Cr/Au, 5/25 nm) were deposited in each corner via thermal evaporation through a shadow mask. OECT samples were prepared on the same substrates using double-layer liftoff photolithography, using thicker contacts (Cr/Au, 5/200 nm) to ensure a small series resistance (see OECT details below). Samples for GIWAXS measurement were prepared on Si (native oxide) and cleaned using the same procedure. FTIR samples were coated onto double side polished undoped Si, also cleaned using the above procedure. Substrates were cleaned by sequential sonication in 2% Decon 90/DI water, DI water, acetone, and isopropanol, then dried with nitrogen flow and exposed to oxygen plasma (300 W, 10 min) before use.

PBTTT films were spin coated from 80 °C solutions using preheated glass pipettes onto 80 °C substrates. Samples were spun at 1500 rpm until dry (60 s) and subsequently annealed in N$_2$ at 180 °C for 20 min, then slowly cooled to room temperature by switching off the hotplate.

Ion-exchange doping solutions were prepared immediately before use due to the limited stability of many dopants in the presence of dilute water impurities. To obtain a standard 100:1 × 10^{-3} M electrolyte:dopant concentration, electrolyte stock solutions (1 M) and oxidizer stock solutions (10 × 10^{-3} M) were mixed with acetonitrile at 1:1:8 ratio,

respectively. Samples were sequentially doped with 150 µL doping solution per cm^2 substrate area, waiting a variable delay period, then spinning off the excess solution at 8000 rpm. While spinning, samples were washed with 1 mL acetonitrile to remove excess electrolyte and dopant from the surface.

Conductivity Measurements: Conductivity was measured in van der Pauw configuration.[66,67] Measurements were performed using an Agilent 4155B sourcemeter under nitrogen atmosphere (<20 ppm O$_2$). Four measurements were performed per sample by measuring a 2-point *I–V* hysteresis sweep (−0.1 to 0.1 V) between each pair of adjacent electrodes, while simultaneously monitoring the voltage at the remaining two electrodes. The resulting four point resistance data was checked for hysteresis, current reversal, and reciprocity $\left(\frac{V_{12}}{V_{34}} = \frac{V_{34}}{V_{12}}\right)$ to a tolerance of 3%, in line with NIST recommendations.[68] Uncertainties were dominated by thickness uncertainty; contact size effects contribute <1% to the relative error.[66,67] Thickness measurements were performed using a Bruker Dektak XT. Conductivity values were calculated using the undoped film thickness to prevent thickness variations from creating apparent differences in charge transport properties between samples.

OECT Measurements: OECT devices were measured in a two point geometry. After spin coating the polymer onto substrates with pre-patterned electrodes, the polymer layer was removed to define the device active area. Device length was 4000 µm; widths varied between devices and were measured via surface profilometry after measurement (650–1200 µm, standard deviation < 50 µm within each device). Thick electrodes (5/200 nm Ti/Au) were used to reduce the total series resistance to 65 Ω; the minimum device resistance measured was 1600 Ω.

PDMS spacers (3 mm thick) were prepared with Sylgard 184 10:1 w/w base to crosslinker ratio and baked at 60C for 1.5 h in an oven. The spacers were patterned to expose the active area and then immersed in acetonitrile overnight to remove any residual crosslinker. To form the OECT, a silver quasi-reference electrode identical to those used in our CV measurements (Ag oxidized by O$_2$ plasma 300 W, 1 min) was pierced through the side of a spacer, then placed on top of the device substrate and filled with electrolyte (100 × 10^{-3} M BMP TFSI in AN) under nitrogen atmosphere (<1 ppm H$_2$O, O$_2$). The electrolyte well was sealed with a Pt sheet acting as the gate electrode, and clamped together between two acrylic sheets. The resulting assembly remained airtight for over 24 h.

After sealing the device, measurements were performed in air using an Agilent 4155B sourcemeter. Source drain *I–V* measurements used a voltage range from −0.1 to 0.1 V. Gate voltage was swept from 0 to 1.3 V and back in 0.1 V increments. Before the *I–V* measurement at each gate voltage, the device was held with the gate on and 0 V source–drain voltage for a hold time (varying between 60 and 300 s; see Figure 5d). The hold time was fixed for each gate voltage sweep; new devices were used for each different hold time measurement. The potential of the silver reference was measured during each *I–V* measurement, which was converted to V versus Fc/Fc$^+$ using a separate CV measurement.

Spectroscopy: UV–vis–NIR spectra were collected on a Shimadzu UV-3600i dual beam spectrometer, using a 3 nm slit width and 2 nm data interval. Substrate background spectra were collected separately. IR (<0.75 eV) and UV (>3.02 eV) regions were smoothed using a Savitzky–Golay filter;[69] the filter window was 50 points in the IR and 10 points in the UV. FTIR spectra were collected on a Bruker Vertex 70V using a DLaTGS detector.

GIWAXS Characterization: GIWAXS measurements were performed at Beamline 8-ID-E at the Advanced Photon Source at Argonne National Laboratory. Samples were irradiated with a 10.9 keV X-ray at an incidence angle 0.13° for 2 summed exposures of 2.5 s (5 s of exposure in total), and scattered X-rays were recorded by a Pilatus 1 M detector located 228.16 mm from the sample. The collected images were then processed by using the GIXSGUI software.[70] The background was subtracted by fitting the curves to an exponential decay, and peaks were fitted to Gaussian functions. Peak widths and positions were used to calculate the π–π paracrystallinity assuming the coherence length is dominated by paracrystalline disorder, as previously suggested by Rivnay et al.:[71]

$$g = \frac{1}{2\pi} \sqrt{\Delta_q \, d_{hkl}} \qquad (6)$$

where Δ_q is the diffraction peak full width at half maximum, and d_{hkl} is the interplanar distance.

Supporting Information

Supporting Information is available from the Wiley Online Library or from the author.

Conflict of Interest

The authors declare no conflict of interest.

Data Availability Statement

The data that support the findings of this study are openly available at the Apollo University of Cambridge repository at https://doi.org/10.17863/CAM.72495.

[1] I. Salzmann, G. Heimel, M. Oehzelt, S. Winkler, N. Koch, *Acc. Chem. Res.* **2016**, *49*, 370.

[2] I. E. Jacobs, A. J. Moulé, *Adv. Mater.* **2017**, *29*, 1703063.

[3] B. Lüssem, C.-M. Keum, D. Kasemann, B. Naab, Z. Bao, K. Leo, *Chem. Rev.* **2016**, *116*, 13714.

[4] W. Zhao, J. Ding, Y. Zou, C.-a. Di, D. Zhu, *Chem. Soc. Rev.* **2020**, *49*, 7210.

[5] I. E. Jacobs, F. Wang, N. Hafezi, C. Medina-Plaza, T. F. Harrelson, J. Li, M. P. Augustine, M. Mascal, A. J. Moulé, *Chem. Mater.* **2017**, *29*, 832.

[6] J. Fuzell, I. E. Jacobs, S. Ackling, T. F. Harrelson, D. M. Huang, D. Larsen, A. J. Moulé, *J. Phys. Chem. Lett.* **2016**, *122*, 4297.

[7] J. Li, I. Duchemin, O. M. Roscioni, P. Friederich, M. Anderson, E. Da Como, G. Kociok-Köhn, W. Wenzel, C. Zannoni, D. Beljonne, X. Blase, G. D'Avino, *Mater. Horiz.* **2019**, *6*, 107.

[8] I. Salzmann, G. Heimel, S. Duhm, M. Oehzelt, P. Pingel, B. M. George, A. Schnegg, K. Lips, R.-P. Blum, A. Vollmer, N. Koch, *Phys. Rev. Lett.* **2012**, *108*, 035502.

[9] A. Hamidi-Sakr, L. Biniek, J.-L. Bantignies, D. Maurin, L. Herrmann, N. Leclerc, P. Lévêque, V. Vijayakumar, N. Zimmermann, M. Brinkmann, *Adv. Funct. Mater.* **2017**, *27*, 1700173.

[10] K. Kang, S. Watanabe, K. Broch, A. Sepe, A. Brown, I. Nasrallah, M. Nikolka, Z. Fei, M. Heeney, D. Matsumoto, *Nat. Mater.* **2016**, *15*, 896.

[11] D. T. Scholes, P. Y. Yee, J. R. Lindemuth, H. Kang, J. Onorato, R. Ghosh, C. K. Luscombe, F. C. Spano, S. H. Tolbert, B. J. Schwartz, *Adv. Funct. Mater.* **2017**, *27*, 1702654.

[12] I. E. Jacobs, C. Cendra, T. F. Harrelson, Z. I. Bedolla Valdez, R. Faller, A. Salleo, A. J. Moulé, *Mater. Horiz.* **2018**, *5*, 655.

[13] K. E. Watts, B. Neelamraju, E. L. Ratcliff, J. E. Pemberton, *Chem. Mater.* **2019**, *31*, 6986.

[14] V. I. Arkhipov, E. V. Emelianova, P. Heremans, H. Bässler, *Phys. Rev. B* **2005**, *72*, 235202.

[15] P. Pingel, D. Neher, *Phys. Rev. B* **2013**, *87*, 115209.

[16] M. L. Tietze, J. Benduhn, P. Pahner, B. Nell, M. Schwarze, H. Kleemann, M. Krammer, K. Zojer, K. Vandewal, K. Leo, *Nat. Commun.* **2018**, *9*, 1182.

[17] M. Schwarze, C. Gaul, R. Scholz, F. Bussolotti, A. Hofacker, K. S. Schellhammer, B. Nell, B. D. Naab, Z. Bao, D. Spoltore, K. Vandewal, J. Widmer, S. Kera, N. Ueno, F. Ortmann, K. Leo, *Nat. Mater.* **2019**, *18*, 242.

[18] T. J. Aubry, J. C. Axtell, V. M. Basile, K. J. Winchell, J. R. Lindemuth, T. M. Porter, J.-Y. Liu, A. N. Alexandrova, C. P. Kubiak, S. H. Tolbert, A. M. Spokoyny, B. J. Schwartz, *Adv. Mater.* **2019**, *31*, 1805647.

[19] A. Fediai, F. Symalla, P. Friederich, W. Wenzel, *Nat. Commun.* **2019**, *10*, 4547.

[20] Y. Xuan, X. Liu, S. Desbief, P. Leclère, M. Fahlman, R. Lazzaroni, M. Berggren, J. Cornil, D. Emin, X. Crispin, *Phys. Rev. B* **2010**, *82*, 115454.

[21] D. Neusser, C. Malacrida, M. Kern, Y. M. Gross, J. van Slageren, S. Ludwigs, *Chem. Mater.* **2020**, *32*, 6003.

[22] N. G. Connelly, W. E. Geiger, *Chem. Rev.* **1996**, *96*, 877.

[23] M. Armand, F. Endres, D. R. MacFarlane, H. Ohno, B. Scrosati, *Nat. Mater.* **2009**, *8*, 621.

[24] Y. Yamashita, J. Tsurumi, M. Ohno, R. Fujimoto, S. Kumagai, T. Kurosawa, T. Okamoto, J. Takeya, S. Watanabe, *Nature* **2019**, *572*, 634.

[25] H. Kato, S. Takemura, Y. Nakajima, *Thin Solid Films* **1998**, *317*, 367.

[26] V. Carlier, M. Skompska, C. Buess-Herman, *J. Electroanal. Chem.* **1998**, *456*, 139.

[27] R.-Q. Png, M. C. Ang, M.-H. Teo, K.-K. Choo, C. G. Tang, D. Belaineh, L.-L. Chua, P. K. Ho, *Nat. Commun.* **2016**, *7*, 11948.

[28] S.-J. Wang, D. Venkateshvaran, M. R. Mahani, U. Chopra, E. R. McNellis, R. Di Pietro, S. Schott, A. Wittmann, G. Schweicher, M. Cubukcu, K. Kang, R. Carey, T. J. Wagner, J. N. M. Siebrecht, D. P. G. H. Wong, I. E. Jacobs, R. O. Aboljadayel, A. Ionescu, S. A. Egorov, S. Mueller, O. Zadvorna, P. Skalski, C. Jellett, M. Little, A. Marks, I. McCulloch, J. Wunderlich, J. Sinova, H. Sirringhaus, *Nat. Electron.* **2019**, *2*, 98.

[29] C. Y. Kao, B. Lee, L. S. Wielunski, M. Heeney, I. McCulloch, E. Garfunkel, L. C. Feldman, V. Podzorov, *Adv. Funct. Mater.* **2009**, *19*, 1906.

[30] S. N. Patel, A. M. Glaudell, D. Kiefer, M. L. Chabinyc, *ACS Macro Lett.* **2016**, *5*, 268.

**ADVANCED
SCIENCE NEWS**
www.advancedsciencenews.com

**ADVANCED
MATERIALS**
www.advmat.de

[31] D. Yuan, L. Liu, X. Jiao, Y. Zou, C. R. McNeill, W. Xu, X. Zhu, D. Zhu, *Adv. Sci.* **2018**, *5*, 1800947.

[32] F. G. Helfferich, *Ion Exchange*, Courier Corporation, North Chelmsford, MA, USA **1995**.

[33] I. E. Jacobs, E. W. Aasen, J. L. Oliveira, T. N. Fonseca, J. D. Roehling, J. Li, G. Zhang, M. P. Augustine, M. Mascal, A. J. Moule, *J. Mater. Chem. C* **2016**, *4*, 3454.

[34] J. Li, C. Koshnick, S. O. Diallo, S. Ackling, D. M. Huang, I. E. Jacobs, T. F. Harrelson, K. Hong, G. Zhang, J. Beckett, M. Mascal, A. J. Moulé, *Macromolecules* **2017**, *50*, 5476.

[35] J. H. Burke, M. J. Bird, *Adv. Mater.* **2019**, *31*, 1806863.

[36] C. Moreau, G. Douhéret, *J. Chem. Thermodyn.* **1976**, *8*, 403.

[37] C. Zhong, Y. Deng, W. Hu, J. Qiao, L. Zhang, J. Zhang, *Chem. Soc. Rev.* **2015**, *44*, 7484.

[38] W. Zhao, J. Sun, *Chem. Rev.* **2018**, *118*, 10349.

[39] T. L. Murrey, M. A. Riley, G. Gonel, D. D. Antonio, L. Filardi, N. Shevchenko, M. Mascal, A. J. Moulé, *J. Phys. Chem. Lett.* **2021**, *12*, 1284.

[40] G. J. Brealey, N. Uri, *J. Chem. Phys.* **1952**, *20*, 257.

[41] T. B. Swanson, V. W. Laurie, *J. Phys. Chem.* **1965**, *69*, 244.

[42] M. Galiński, A. Lewandowski, I. Stepniak, *Electrochim. Acta* **2006**, *51*, 5567.

[43] B. Kratochvil, R. Long, *Anal. Chem.* **1970**, *42*, 43.

[44] M. Magini, T. Radnai, *J. Chem. Phys.* **1979**, *71*, 4255.

[45] W. Liu, B. Etschmann, J. Brugger, L. Spiccia, G. Foran, B. McInnes, *Chem. Geol.* **2006**, *231*, 326.

[46] Z. Liang, Y. Zhang, M. Souri, X. Luo, A. M. Boehm, R. Li, Y. Zhang, T. Wang, D.-Y. Kim, J. Mei, S. R. Marder, K. R. Graham, *J. Mater. Chem. A* **2018**, *6*, 16495.

[47] Y. Shimura, R. Tsuchida, *Bull. Chem. Soc. Jpn.* **1956**, *29*, 311.

[48] D. O. Whittemore, D. Langmuir, *J. Chem. Eng. Data* **1972**, *17*, 288.

[49] S. Trasatti, *Pure Appl. Chem* **1986**, *58*, 955.

[50] C. M. Cardona, W. Li, A. E. Kaifer, D. Stockdale, G. C. Bazan, *Adv. Mater.* **2011**, *23*, 2367.

[51] R. R. Gagne, C. A. Koval, G. C. Lisensky, *Inorg. Chem.* **1980**, *19*, 2854.

[52] Y. Karpov, T. Erdmann, I. Raguzin, M. Al-Hussein, M. Binner, U. Lappan, M. Stamm, K. L. Gerasimov, T. Beryozkina, V. Bakulev, D. V. Anokhin, D. A. Ivanov, F. Günther, S. Gemming, G. Seifert, B. Voit, R. Di Pietro, A. Kiriy, *Adv. Mater.* **2016**, *28*, 6003.

[53] M. Bešter-Rogač, A. Stoppa, R. Buchner, *J. Phys. Chem. B* **2014**, *118*, 1426.

[54] Q. Zhang, Y. Sun, W. Xu, D. Zhu, *Energy Environ. Sci.* **2012**, *5*, 9639.

[55] H. Tanaka, S. Nishio, H. Ito, S.-i. Kuroda, *Appl. Phys. Lett.* **2015**, *107*, 243302.

[56] J. L. Bredas, G. B. Street, *Acc. Chem. Res.* **1985**, *18*, 309.

[57] R. Ghosh, F. C. Spano, *Acc. Chem. Res.* **2020**, *53*, 2201.

[58] C. G. Bischak, L. Q. Flagg, K. Yan, T. Rehman, D. W. Davies, R. J. Quezada, J. W. Onorato, C. K. Luscombe, Y. Diao, C.-Z. Li, D. S. Ginger, *J. Am. Chem. Soc.* **2020**, *142*, 7434.

[59] I. McCulloch, M. Heeney, C. Bailey, K. Genevicius, I. MacDonald, M. Shkunov, D. Sparrowe, S. Tierney, R. Wagner, W. Zhang, M. L. Chabinyc, R. J. Kline, M. D. McGehee, M. F. Toney, *Nat. Mater.* **2006**, *5*, 328.

[60] R. J. Kline, D. M. DeLongchamp, D. A. Fischer, E. K. Lin, L. J. Richter, M. L. Chabinyc, M. F. Toney, M. Heeney, I. McCulloch, *Macromolecules* **2007**, *40*, 7960.

[61] Y. Karpov, N. Kiriy, M. Al-Hussein, M. Hambsch, T. Beryozkina, V. Bakulev, S. C. B. Mannsfeld, B. Voit, A. Kiriy, *Chem. Commun.* **2018**, *54*, 307.

[62] P. K. Koech, A. B. Padmaperuma, L. Wang, J. S. Swensen, E. Polikarpov, J. T. Darsell, J. E. Rainbolt, D. J. Gaspar, *Chem. Mater.* **2010**, *22*, 3926.

[63] A. Davison, N. Edelstein, R. Holm, A. Maki, *J. Am. Chem. Soc.* **1964**, *86*, 2799.

[64] S. A. Paniagua, J. Baltazar, H. Sojoudi, S. K. Mohapatra, S. Zhang, C. L. Henderson, S. Graham, S. Barlow, S. R. Marder, *Mater. Horiz.* **2014**, *1*, 111.

[65] T. Fukunaga, *J. Am. Chem. Soc.* **1976**, *98*, 610.

[66] R. Chwang, B. J. Smith, C. R. Crowell, *Solid-State Electron.* **1974**, *17*, 1217.

[67] D. W. Koon, *Rev. Sci. Instrum.* **1989**, *60*, 271.

[68] N. D. C. D. NIST Physical Measurement Laboratory, Resistivity and Hall Measurements, www.nist.gov/pml/nanoscale-device-characterization-division/popular-links/hall-effect/resistivity-and-hall (accessed: January 2021).

[69] A. Savitzky, M. J. E. Golay, *Anal. Chem.* **1964**, *36*, 1627.

[70] Z. Jiang, *J. Appl. Crystallogr.* **2015**, *48*, 917.

[71] J. Rivnay, R. Noriega, R. J. Kline, A. Salleo, M. F. Toney, *Phys. Rev. B* **2011**, *84*, 045203.

2102988 (12 of 12)